energy&fuels

pubs.acs.org/EF

Article

Impact of Operational Parameters on the CO_2 Absorption Rate in $Ca(OH)_2$ Aqueous Carbonation—Implications for Process Efficiency

Quentin Wehrung,* Linda Pastero, Davide Bernasconi, Andrea Cotellucci, Marco Bruno, Simona Cavagna, Enrico Destefanis, Caterina Caviglia, and Alessandro Pavese

Cite This: *Energy Fuels* 2024, 38, 16678−16691

Read Online

ACCESS | Metrics & More | Article Recommendations | Supporting Information

ABSTRACT: The impact of operational parameters on the CO_2 absorption rate ($\eta(t)$) during $Ca(OH)_2$ aqueous carbonation has been investigated, including the reagent concentration, CO_2 volumetric flow rate, temperature, Na- and K-salt impurity concentration, ionic strength, and mixing system. The carbonation mechanisms were numerically investigated with the modeling tool Phreeqc. Positive correlations were predicted and confirmed between $\eta(t)$ and $Ca(OH)_2$ initial concentrations, reduced volumetric flow rate, elevated temperature, and less obvious parameters like salt impurities and increased ionic strength. The present results indicate a modest impact (a few percent increase) on the absorption rate when varying $Ca(OH)_2$ concentration from 1 to 10 wt %. Increasing the temperature from 283 to 363 K enhances the $\eta(t)$ of about 37%. The average seawater NaCl concentration (3.5 wt %) enhances $\eta(t)$ values by as much as 75%. Na_2SO_4 and K_2SO_4 in place of NaCl and KCl, respectively, suggest that sulfate ions promote the dissolution of CO_2 in aqueous solutions more efficiently than chloride ions. We demonstrate that the CO_2−water interfacial surface area plays a crucial role, causing a cascade of kinetic acceleration of dissolution. Utilizing a static mixer (sparger and porous stone diffusor) significantly accelerates dissolution−precipitation, leading to enhanced absorption rates and reducing energy consumption associated with mixing. This approach, coupled with 3.5 wt % NaCl concentration, achieves a CO_2 absorption rate of up to 90% for a 2 L/min CO_2 flow. The proven enhancements pave the way for more efficient reactor design tailored for ex situ carbon capture both "at the smokestack" and potentially for direct air capture.

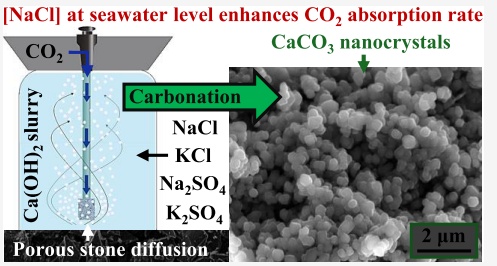

1. INTRODUCTION

The urgent need to mitigate carbon dioxide (CO_2) emissions and address climate change has propelled the exploration of innovative approaches for carbon capture and storage (CCS). Among these, the aqueous carbonation of calcium hydroxide ($Ca(OH)_2$) emerges as a promising avenue for ex situ applications,[1] given that this reactant supplies both alkalinity (OH^-) and reactive divalent cations (Ca^{2+}) to readily precipitate stable calcium carbonate ($CaCO_3$). Its fast dissolution enables the absorption of a substantial proportion of CO_2 from gas streams continuously flowing through CCS reactors.[2] $Ca(OH)_2$ carbonation thus constitutes a pivotal mechanism for wide-ranging CCS applications, including the calcium looping (CaL) methods[3] and industrial alkaline waste (IAW) carbonation.[4−7] Renforth[8] points out that IAWs will collectively have a CCS potential of 2.9−8.5 billion tonnes per year by 2100, potentially supplying a significant portion of the negative emissions needed to limit the global temperature rise to below 2 °C.

Typical IAWs of interest include air pollution control residues (APC) and fly ashes (FA) from municipal solid waste incineration (MSWI),[9] cement kiln dusts (CKD),[10] steel slags,[11,12] high-calcium coal fly ashes (HCFA),[13] waste paper fly ashes (WPFA),[14] and calcium carbide residues (CCR).[15] In these byproducts, calcium is a predominant element, occurring in various amounts as free CaO, $Ca(OH)_2$, CaClOH, and $CaCl_2{\cdot}xH_2O$ as well as Ca-bearing silicates and glasses. Given that calcium (chloro)(hydr-)oxides (CCHO) dissolve orders of magnitude faster than silicates and glasses, the aqueous carbonation pathways involving these phases play a primary role in controlling the rate of CO_2 absorption, along with CO_2 dissolution. Moreover, IAWs are typically landfilled, posing long-term health and environmental risks. The management of these wastes is a growing concern, and aqueous carbonation offers a viable solution by simultaneously washing, stabilizing, and facilitating their reuse as construction aggregates.[16] Indeed, aqueous carbonation with $Ca(OH)_2$ is recognized as an efficient technique for stabilizing heavy metals in IAWs, such as As, Ba, Cd, Cu, Hg, Pb, Se, Sr, and Zn, through coprecipitation and adsorption.[16−22]

Received: May 23, 2024
Revised: August 13, 2024
Accepted: August 14, 2024
Published: August 22, 2024

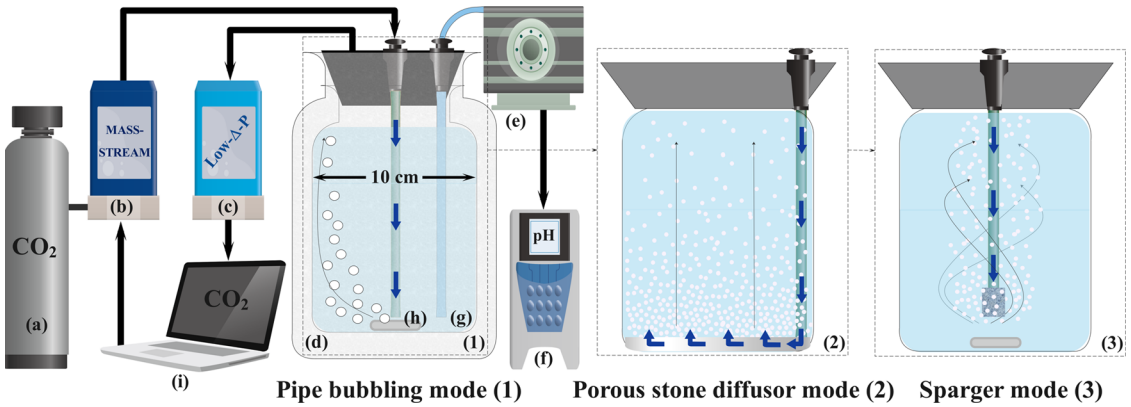

Figure 1. Modular experimental setup during carbonation experiments. The bold blue and thin black arrows indicate the CO_2 flow. The bubble size and spatial distribution in the reactor column are schematically compared between (1) standard CO_2 bubbling with a magnetic stirrer, (2) addition of a porous stone diffusor, (3) addition of a porous stone sparger, (a) gas tank, (b) valve, (c) flow meter, (d) double-wall pyrex reactor, (e) peristaltic pump, (f) pH/EC meters, (g) $Ca(OH)_2$ aqueous suspension, (h) stirrer, and (i) computer with remotely adjustable control settings for gas flow sensors.

When designing carbonation reactors, a primary difficulty lies in enhancing the CO_2 absorption rate, irrespective of the nature of the gas stream, whether it is flue gas, pure CO_2, or even air. Enhancing the CO_2 absorption rates has the potential of mitigating the CO_2 emissions of stationary point sources for efficient IAW carbonation processes as well as lowering the energy consumption of direct air capture (DAC). In the case of $Ca(OH)_2$ and other CCHO, the subsequent increase in carbonation kinetics results in the formation of smaller calcium carbonate ($CaCO_3$) crystals. This leads to a larger surface area, more reaction sites, and potentially a higher dissolution rate. This is particularly significant when pushing the reaction further, as observed in CaL methods or in accelerated weathering of limestone (AWL).[23,24]

An additional challenge arises from the substantial water demand of carbon capture processes.[25] Given that freshwater use has surpassed planetary boundaries, declared by the Stockholm Resilience Center in 2023,[26] CCS must turn to alternative water sources, particularly seawater and various industrial wastewaters. Seawater stands out as a primary option for CO_2 mitigation from point sources in coastal areas, with the concentration of NaCl being a key factor influencing the CO_2 absorption rates. Wastewaters encompass those from coke ovens, pickling and cooling processes (steel production), stormwater runoff, process and wash waters (cement production), and flue gas-cleaning waters and bottom ash leachates. Furthermore, in instances of water reuse during IAW carbonation, it is established that the concentrations of Na^+, K^+, and Cl^- gradually increase.[27] However, the specific impact on the CO_2 removal efficiency remains unexplored. Impurities, originating from flue gas with dissolved acid gases like SO_2, NO_2, or HCl, as well as particulate matters such as fly ashes accumulating in carbonation reactors, also play a role.[28] Therefore, it is crucial to clarify the impact of salinity and the presence of sodium, potassium, chlorides, and sulfate impurities on CO_2 absorption rates. Thus, NaCl, KCl, Na_2SO_4, and K_2SO_4 were selected for the investigation.

In the pursuit of designing efficient carbonation scrubbers, a pivotal consideration lies in selecting the optimal mixing system. This choice must strike a delicate balance involving boosting the CO_2 absorption rates and minimizing the energy requirements and maintenance needs. Achieving a synthesis between these considerations poses a complex challenge. All these aspects have motivated numerous studies to model the precipitation of calcium carbonate.[29−32]

This work aims to contribute to the optimization of carbonation scrubber design by providing a study about the relevant factors influencing the CO_2 absorption rate during $Ca(OH)_2$ aqueous carbonation in open systems. The detailed exploration of the operational parameters allows one to plan efficient strategies, addressing the critical question "how to optimize a carbonation scrubber to absorb the flowing CO_2 as fast as possible?". The investigated operational parameters include the following:

- Portlandite ($Ca(OH)_2$) initial concentration.
- CO_2 flow rate.
- Temperature.
- NaCl, KCl, Na_2SO_4, and K_2SO_4 concentrations (salinity).
- Static gas−liquid mixing system, with a comparison of the pipe, sparger, and porous stone diffusor.

An experimental dataset, based on batch experiments, was collected using high-precision gas flow sensors to measure the percentage of flowing CO_2 absorbed by the reagents under a wide range of operational conditions. Equilibrium and dissolution kinetic models were developed using Phreeqc to help us interpret the CO_2 absorption vs time patterns. The present study provides a novel contribution to the existing literature by introducing a new and accurate quantification method to assess the effects of chemical factors (reagent concentrations, chloride, and sulfate ions) and physical variables (flow rate, temperature, and mixing system design) on the CO_2 absorption rate in $Ca(OH)_2$ aqueous carbonation. Earlier investigations did not quantify the impact of chlorides, particularly NaCl, despite their crucial importance given the expected widespread use of seawater in carbonation systems.

2. MATERIALS AND METHODS

2.1. Chemical Reagents. $Ca(OH)_2$ was provided by ERBApharm at a purity of 98%. Observation by scanning electron microscopy (SEM) showed that the particles have rough surfaces and a layered morphology, as shown in Supporting Information Figure S1. $Ca(OH)_2$ had a specific surface area (SSA) equal to 16.0351 m^2/g ± 0.0907 (R^2 = 0.999). CO_2 was provided by Sapio at a purity of 99.9%. All other solid chemical salts were provided by Sigma-Aldrich. Ultrapure and degassed water was used in the experiments.

https://doi.org/10.1021/acs.energyfuels.4c02455
Energy Fuels 2024, 38, 16678−16691

2.2. Laboratory Equipment. CO_2 flows were controlled and measured by a Bronkhorst modular system, composed of a mass flow controller ("*valve*" hereafter) (MFC D-6321), with a maximum flow range of 2 L_n/min CO_2 and accuracy of ±1.0% relative deviation ("*RD*" hereafter) plus ±0.5% full scale (FS hereafter) and a low-ΔP ("*flow meter*" hereafter) F101E (max flow range of 3 L_n/min CO_2 and accuracy ±1.0% FS). A digital pc board provides self-diagnostics, alarm and counter functions, digital communication (RS232), and remotely adjustable control settings, and an on-board interface based on the FLOW-BUS protocol makes it possible to communicate via a multibus system. CO_2 absorption acquisition data were characterized every 0.25−5 s according to the specific accuracy requirements of the experimental run. pH and EC (electrolytical conductivity, μS/cm) of the samples were measured by a Hanna HI H-ORP meter and a Mettler Toledo Five Easy EC-meter, respectively. The samples' masses were measured with a precision of ±0.1%. Air-free experiments were prepared under a N_2 atmosphere using an ITECO SGS20 "inert gas" glovebox to avoid early CO_2 absorption.

Scanning electron microscopy (SEM) imaging was conducted utilizing a TESCAN VEGA, equipped with secondary electron (SE) and backscattered electron (BSE) detectors. Typical experimental settings included operation with a tungsten (W) filament, an accelerating voltage of 10 kV, and a working distance of 5 mm.

X-ray powder diffraction (XRPD) measurements for the qualitative identification of the crystalline phases were carried out using a Rigaku MiniFlex 600 benchtop X-ray diffractometer (Bragg−Brentano geometry, Cu Kα radiation, X-ray source operating at 600 W (40 kV, 15 mA); D/teX Ultra2 silicon strip detector; $3° < 2\theta < 75°$, step width 0.02°, scan speed 4°/min).

Specific surface area (SSA) analysis was performed using a Micromeritics ASAP 2020 instrument employing the Brunauer−Emmett−Teller (BET) method with N_2 adsorption at −196 °C. Prior to the measurement, samples underwent degassing at 150 °C for 240 min.

2.3. Experimental Procedures. Each experiment was conducted on the setup represented in Figure 1, using a double-wall pyrex reactor of 1.5 L. The porous stone diffusor was an Ultramicro nanoatomized bubble plate B-80 with a diameter of 80 mm × 11 mm height. The sparger constituted of a porous stone cylinder with a diameter of 25 mm x 40 mm height. Figure 1 illustrates the diverse modes of the modular experimental setup employed in this study, juxtaposing the standard bubbling configuration with the diffusor and sparger setup. In Table 1, the investigated experimental parameters are summarized with their operational ranges. Detailed experimental conditions are provided in Table S1 with the corresponding identifiers. Experimental runs were performed by changing the operational parameters one by one to isolate their impact on the CO_2 absorption rate. Specific conditions were carefully selected to optimize the representativity of each parameter investigated.

Table 1. Overview of the Experimental Parameters and Their Corresponding Range

variables	units	ranges/types
water mass	kg	0.5−1.2
liquid-to-solid ratio		10−66.7
$Ca(OH)_2$ initial concentration	wt %	1−10
CO_2 volumetric flow rate	L/min	0.3−2
temperature	K	283−363
NaCl concentration	wt %	0−20
KCl concentration	wt %	0−20
Na_2SO_4 concentration	wt %	0−8
K_2SO_4 concentration	wt %	0−4
static gas−liquid mixer		pipe, sparger, diffusor
constants		**values**
$Ca(OH)_2$ initial SSA	m^2/g	16.0351
pressure	bar	1.2
CO_2 concentration	vol %	100
stirrer speed	rpm	300
cylinder height × diameter	cm	16.8 × 10

Preliminary tests proved that two portlandite carbonation runs were sufficient to accurately represent the performances under the experimental conditions. Several series of "blank" experiments were performed with ultrapure water and an empty reactor, using the procedures described in the ensuing sections, to correctly calibrate the setup. A linear proportionality was observed to hold between flow measurements at the valve and flow meter, so that $FLOW\_BLANK_{valve} = k_{cal} \cdot FLOW\_BLANK_{flow\ meter}$.

2.4. Portlandite Carbonation. 101 experiments were conducted, namely, A0−5, B0−5, C0−5, T1−9, SPR1−5, SPR_Na1−5, Diff1−4, NaCl1−20, KCl1−17, NaSO1−15, and KSO1−8, as shown by Table S1. Reactants were combined with the ultrapure water in given amounts under a N_2 atmosphere. Subsequently, the suspension was poured into the reactor. The solution was stirred thoroughly for at least 10 min to ensure proper mixing of the $Ca(OH)_2$ suspension. Precise control over solution temperature was achieved using a thermostatic bath connected to the reactor's double wall, and the temperature was monitored directly within the solution via a PT100 thermocouple. In the instance of experiments T1−9, an extended preparation time was implemented to attain the targeted temperature, reaching up to 363 K. All experiments were executed under a constant CO_2 flow, ranging from 0.3 to 2 L/min. Before each experiment, CO_2 flowed through the reactor to flush out the air. To prevent an immediate reaction between CO_2 and the suspension during the initial flushing step, CO_2 was injected at 2 L/min through a dedicated top-mounted pipe, minimizing gas−liquid contact. The flushing duration was <1 min, resulting in less than 30 mL of CO_2 absorption, which represents 0.1−1% of the total CO_2 uptake during the experiments. At $t = 0$, CO_2 was bubbled into the reactor at the desired flow rate. The experiments reached completion when the flow meter indicated no further CO_2 absorption by the solution ($flow_{valve} = flow_{flow\ meter}$). Each experiment was performed at least in duplicate. Upon completion, a fraction of the samples underwent filtration, drying, and subsequent collection for more analyses.

2.5. Phreeqc Geochemical Models. The PHREEQC-3.7.3[33] program was used for equilibrium and kinetic calculations. The sit.dat database was chosen owing to the elevated salt concentrations in the studied systems, beyond the range of application of the Debye−Hückel theory.[33]

The calcite saturation index (SI), the activities of the ions involved in the calcite precipitation process, and the pH were predicted as a function of the CO_2 absorbed by the system. Two simulations were implemented. In both, a suspension of portlandite (37.5 g) and water (0.5 kg) was used. In one of the two, 17.5 g of NaCl, i.e., 3.5 wt %, was added.

The dissolution kinetic model, implemented in this work for portlandite using the BASIC interpreter embedded in Phreeqc, has already been adopted by several other authors.[24,34,35] The accuracy of the model predictions was assessed by a comparison to the observed rates. The portlandite dissolution rate, saturation ratio of $Ca(OH)_2$, and pH all depend on the amount of water, crystals' surface area $SA(t)$, temperature, Arrhenius pre-exponential factor, and activation energy for dissolution E_a.

The initial surface area SA_0, which was determined by BET, decreases as the reaction proceeds since the particles become smaller in size until they are completely dissolved. This is simulated by calculating the ratio between the initial surface area of portlandite and the amount of undissolved solid remaining after each step, according to the following formula

$$SA(t) = SA_0 \cdot n(t) \cdot a_{exp} \quad (2.1)$$

where $SA(t)$ is the surface area at time t (cm^2); SA_0 is the initial surface area (cm^2/mol); $n(t)$ is the amount of portlandite at time t (mol); and a_{exp} is an empirical parameter ($a_{exp} = 0.6$).[36]

The dissolution rate of portlandite is described by the following equation[36]

https://doi.org/10.1021/acs.energyfuels.4c02455
Energy Fuels 2024, 38, 16678−16691

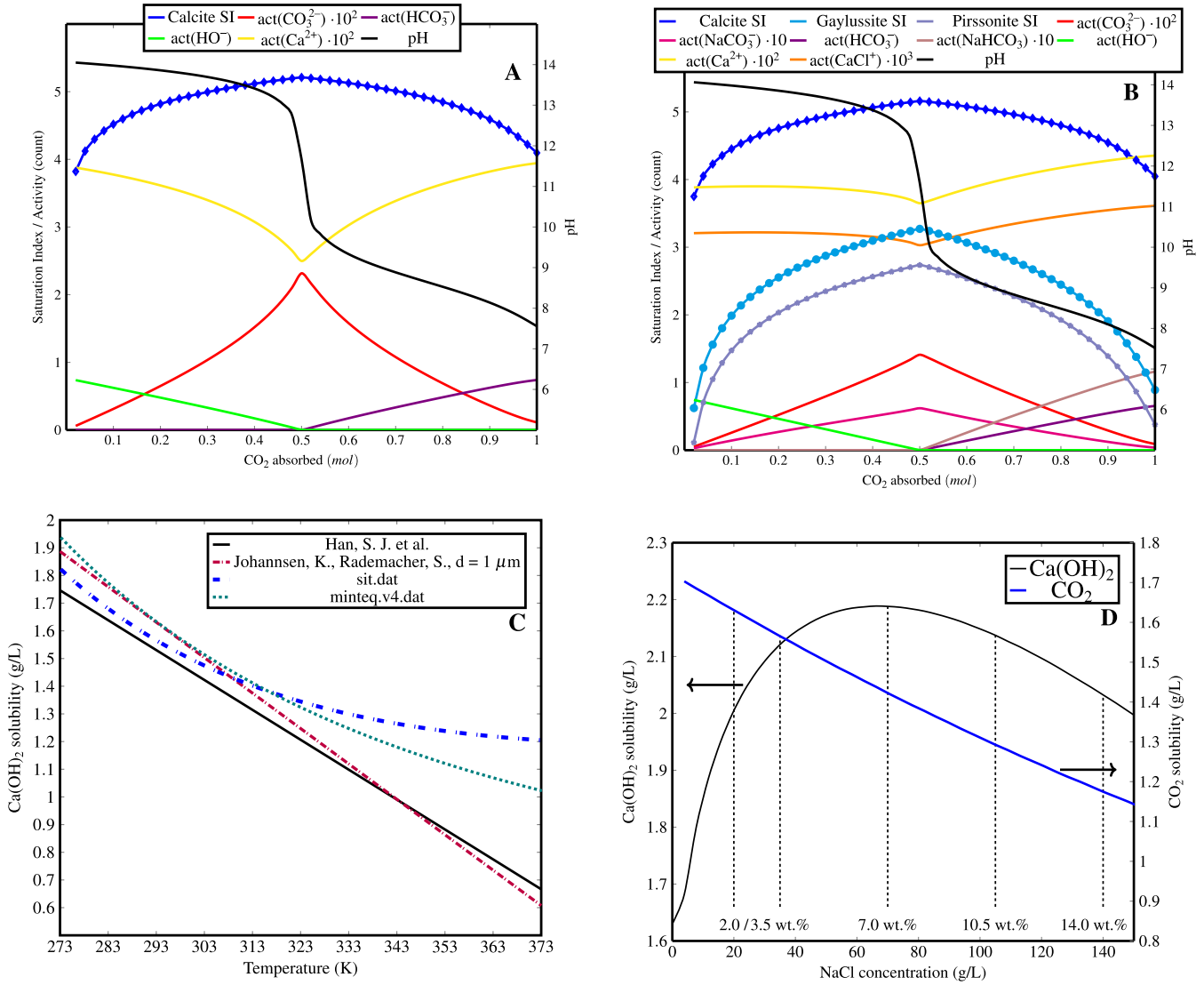

Figure 2. pH, saturation index (SI), and ion activities as a function of absorbed CO_2, calculated using the sit.dat database. (A) Pure $Ca(OH)_2$-H_2O–CO_2 system. (B) Addition of 3.5 wt % NaCl. (C) $Ca(OH)_2$ solubility as a function of temperature. Comparison of experimental equations from the literature with Phreeqc simulations using the sit.dat and minteq v4.dat databases. (D) Solubility of $Ca(OH)_2$ and CO_2 as a function of NaCl concentration calculated using Phreeqc with the Pitzer ion activity model (pitzer.dat). The vertical dashed lines on graph (D) correspond to the typical experimental NaCl concentrations investigated in the study. Phreeqc scripts are provided in the Supporting Information.

$$\text{rate} = (k_1 + k_2 + k_3)\cdot(1 - \Omega)\cdot \text{SA}(t) \tag{2.2}$$

where Ω is the saturation ratio between the ion activity products (IAP) and the solubility product K_{sp} of $Ca(OH)_2$ and k_1, k_2, k_3 are the rate constants, respectively, at acidic, neutral, and alkaline pH

$$k_1 = A\cdot\exp\left(-\frac{E_A}{RT}\right)\cdot a(H^+)^{a_{exp}} \tag{2.3}$$

$$k_2 = A\cdot\exp\left(-\frac{E_A}{RT}\right) \tag{2.4}$$

$$k_3 = A\cdot\exp\left(-\frac{E_A}{RT}\right)\cdot a(HO^-)^{a_{exp}} \tag{2.5}$$

A = pre-exponential factor ($A = 1.39 \cdot 10^{-7}$); E_A = activation energy of dissolution (E_A = 15.188 J·mol^{-1});[37] R = gas constant (R = 8.31451 J·K^{-1}·mol^{-1}); and $a(HO^-)$ and $a(H^+)$ = thermodynamic activities of HO^- and H^+, respectively.

The model was implemented at temperature and [NaCl] ranging between 283–373 K and 0–14 wt %, respectively.

2.6. Data Treatment. The CO_2 absorption rate as a function of time $\eta(t)$ (%) was determined by measuring the influent and effluent CO_2 volumetric flow with the valve and the flow meter placed at the reactor inlet and outlet, respectively. In doing so, the instantaneous absorption rate as a function of time was measured, according to the equation below

$$\eta(t) = 100 \times \left(1 - \frac{k_{cal} \times \mu(t)}{B(t)}\right) \tag{2.6}$$

where $B(t)$ (L/min) = in-flow (valve); $\mu(t)$ (L/min) = out-flow (flow meter); and k_{cal}: calibration factor defined in Section 2.3. Note that η(t) includes the fractions of CO_2 that are either mineralized or dissolved in the active solution.

We introduce the average CO_2 absorption rate over step i of the carbonation run (defined in Section 3.3), $\overline{\eta_i}$ (%), as follows

$$\overline{\eta_i} = \frac{\sum_{t_1}^{t_2} \eta(t)}{n} \tag{2.7}$$

https://doi.org/10.1021/acs.energyfuels.4c02455
Energy Fuels 2024, 38, 16678–16691

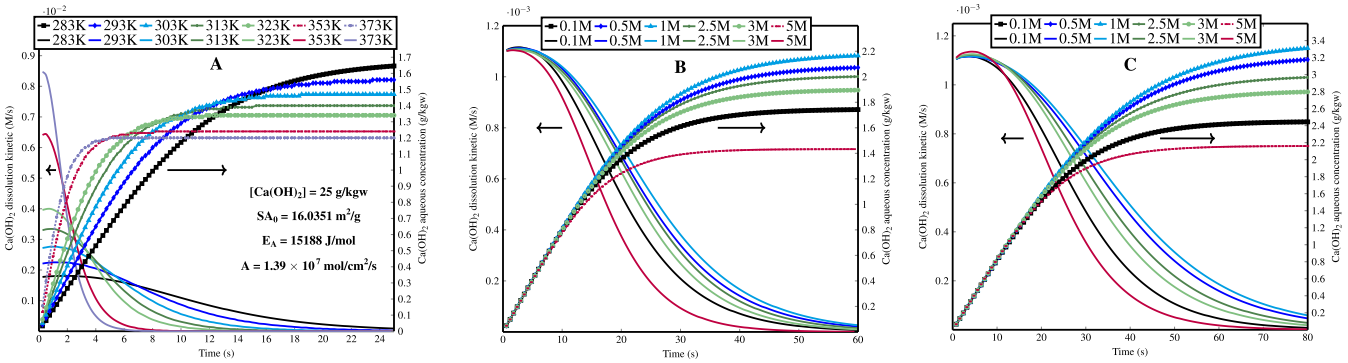

Figure 3. $Ca(OH)_2$ dissolution kinetics (M/s) vs time (s) as a function of (A) temperature (K), (B) NaCl concentration (molality M), and (C) Na_2SO_4 concentration (M) using sit.dat in Phreeqc. The secondary axis shows the $Ca(OH)_2$ aqueous concentration (g/kg of water) nearing equilibrium. The black arrows indicate the axis corresponding to the groups of curves. Note that M stands for molality. Phreeqc scripts are provided in the Supporting Information.

where $[t_1, t_2]$ = interval of time for which $\overline{\eta_i}$ is being calculated, using the methodology detailed in Table S2, and n = size of the studied sample of $\eta(t)$ values.

In addition to $\eta(t)$, we introduce V_{CO_2} (L), the volume of CO_2 absorbed during the interval of time $[t_1, t_2]$.

$$V_{CO_2} = \int_{t_2}^{t_1} \eta(t') \times B(t')dt' \tag{2.8}$$

The ionic strength of the salt solutions was calculated according to

$$I = \frac{1}{2} \times \sum_{i=1}^{n} b_i z_i^2 \tag{2.9}$$

where i = ion identification number; z = charge of ion; and b = molality (m).

The noise in the flow meter data acquisition exhibited a notable escalation with increasing reactor temperatures during experiments T1−9. This phenomenon was attributed to the successive warming (reactor column) and cooling (condensation column) of ascending CO_2, inducing expansion and contraction cycles of the gas phase. To address this, the data acquisition frequency was elevated to 4/s, equating to one acquisition every 0.25 s. This adjustment was made to facilitate the application of a moving average on a representative sample of data, effectively smoothing the CO_2 absorption versus time patterns.

3. RESULTS AND DISCUSSION

3.1. Geochemical Models. *3.1.1. $Ca(OH)_2$ Aqueous Carbonation Equilibrium.* The results shown in Figure 2 demonstrate a significant drop in pH as $Ca(OH)_2$ undergoes reprecipitation to $CaCO_3$, thus depleting the system of the strong base buffering effect against CO_2 acidification. The system shifts from the CO_3^{2-} domain to the HCO_3^- domain, concomitantly with changes in the ion activities. Upon the reaction proceeding, the results indicate a reduction in the calcite saturation index, accompanied by an increase in Ca^{2+} activity and a decrease in the CO_3^{2-} activity. The addition of NaCl (B) causes a significant decrease of the CO_3^{2-} activity in comparison with the pure $Ca(OH)_2$-H_2O−CO_2 system, attributable to the formation of $Na(CO_3)^-$ ions. Notably, the equilibrium of Ca^{2+} is also affected by the formation of new ions such as $CaCl^+$. Overall, the calculated solubilities of calcium hydroxide and the aqueous speciation of Ca^{2+} are in good agreement with earlier measurements.[38] Positive saturation index values are calculated for hydrated sodium−calcium carbonates present in the database, gaylussite ($CaNa_2(CO_3)_2$:$5H_2O$) and pirssonite ($Na_2Ca(CO_3)_2$:$2H_2O$), although these minerals were not detected by XRPD analysis.

The solubility of both CO_2 and portlandite in aqueous sodium chloride solutions has been extensively investigated.[39−41] The results, reported in Figure 2C,D, are in agreement with the experimental values from the literature. Additional results regarding the solubilities of CO_2 and portlandite as functions of KCl, Na_2SO_4, and K_2SO_4 are reported in Supporting Information Figures S7−S9, respectively. Simulations indicate that Na- and K-sulfates increase $Ca(OH)_2$ solubility to a maximum ranging from 3.2 to 4.1 g/L, whereas in the presence of Na- and K-chlorides, portlandite solubility peaks between 2.1 and 2.5 g/L.

3.1.2. $Ca(OH)_2$ Dissolution Kinetics. Despite the increase of temperature, which inherently reduces solubility (Figure 2C) and drives the $Ca(OH)_2$-H_2O system toward equilibrium, the initial $Ca(OH)_2$ dissolution kinetics exhibit a substantial increase (Figure 3A). To understand the relationship between the solubility and dissolution kinetics of portlandite in the present model, we must consider eqs 2.2−2.4. Temperature affects this relationship in two ways: through saturation ratio Ω and rate constants k_i.

For $Ca(OH)_2$, an increase in temperature reduces the solubility product K_{sp}, as described by the van't Hoff equation, due to the exothermic nature of its dissolution. This reduction in K_{sp} causes the saturation ratio Ω to approach unity more quickly, which in turn decreases the term $(1 - \Omega)$ in eq 2.2 faster, therefore slowing the dissolution rate.

Additionally, the rate constants k_i are functions of $\exp\left(\frac{1}{T}\right)$. As temperature rises, the exponential function $\exp\left(-\frac{E_A}{RT}\right)$ increases, resulting in larger rate constants. Thus, as shown by Figure 3A, increasing the temperature initially enhances the dissolution kinetics of $Ca(OH)_2$, leading to even quicker saturation of the solution. This rapid approach to saturation subsequently causes an even faster decline in the dissolution rate. Specifically, at t = 0.25 s, the dissolution kinetics of $Ca(OH)_2$ changes from 1.8×10^{-3} M/s at 283 K to 8.5×10^{-3} M/s at 373 K, while at t = 5 s, these values switch from 1.7×10^{-3} M/s at 283 K to 0.2×10^{-3} M/s at 373 K.

Conversely, the $Ca(OH)_2$ dissolution kinetics do not exhibit an apparent dependency on the Na/K salt concentration (Figure 3B,C and Supporting Information Figure S10). The observed variations in the calculated $Ca(OH)_2$ dissolution kinetic curves in the presence of 0.1−5 m NaCl/Na_2SO_4

https://doi.org/10.1021/acs.energyfuels.4c02455
Energy Fuels 2024, 38, 16678−16691

(Figure 3B,C) are intrinsically linked to fluctuations in $Ca(OH)_2$ solubility, which reaches maximum values of 2.2 and 4 g/L, respectively (Figure 2D and Supporting Information Figure S8). In the present model, the rate constants k_i remain relatively steady in this case. Specifically, at t = 0.6 s in the NaCl solution, the dissolution kinetics of $Ca(OH)_2$ is 1.1 × 10^{-3} M/s at both 1 and 5 M, while at t = 20 s, these values change from 1.5 × 10^{-3} M/s at 1 M to 0.44 × 10^{-3} M/s at 5 M.

3.2. Precipitation Phenomena: General Insights from SEM and XRPD. Calcite precipitation occurred systematically as the unique calcium solid phase in each experiment, irrespective of the presence of additional salt impurities in the initial solution. Thus, it is reasonable to assume total $Ca(OH)_2$ conversion to $CaCO_3$, a conclusion supported by the XRPD and SEM-EDS results. Figure 4 presents the SEM morphological characterization, which reveals the systematic precipitation of nanosized crystals confirmed as calcite by XRPD.

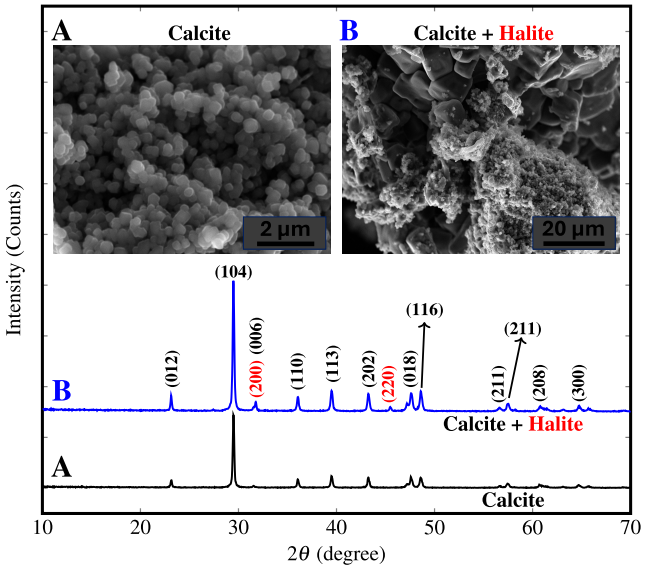

Figure 4. XRPD patterns and SEM images from dried samples collected at completion time for (A) pure $Ca(OH)_2$-H_2O−CO_2 system: results reveal the presence of calcite only and (B) addition of NaCl. Results reveal the presence of both calcite (96.2 wt %) and NaCl (3.8 wt %), with the latter persisting due to the sample being unwashed.

The $Ca(OH)_2$ particles utilized in this investigation exhibit dimensions so small that no passivation of $Ca(OH)_2$ by $CaCO_3$ precipitated occurs at the interfaces of the $Ca(OH)_2$ particles, like several authors report.[42] This may account for the complete conversion of $Ca(OH)_2$ into $CaCO_3$.[43]

3.3. CO_2 Capture Rate vs Time $\eta(t)$: General Insights. The CO_2 absorption rate curves as a function of time allow exploration of the dynamic nature of the absorption process under various conditions. In keeping with the findings of Tiefenthaler,[44] which exhibit a similar qualitative trend between the $\eta(t)$ and precipitation rate of $CaCO_3$ during $Ca(OH)_2$ aqueous carbonation, we observed that $\eta(t)$ is correlated with $CaCO_3$ nucleation frequency in the pure $Ca(OH)_2$-H_2O−CO_2 experiments. To appreciate the impact of the operational variables, Figure 5 divides $\eta(t)$ in four distinct rate-controlling steps (hereafter denoted as step 1: maximum absorption; step 2: first downfall; step 3: secondary absorption; step 4: secondary downfall) according to the methodology detailed in Table S2:

In the pure $Ca(OH)_2$-H_2O−CO_2 system (Figure 5A), the CO_2 absorption rate is controlled by either Ca^{2+} or CO_3^{2-} availability with a complex interplay between both $Ca(OH)_2$ and CO_2 dissolution processes, as described below. CO_3^{2-} availability is affected by both CO_2 dissolution and diffusion kinetics into the bulk solution. In the standard conditions of this study, during carbonation step 1, $Ca(OH)_2$ dissolution is a primary rate driver.[45,46] As the $Ca(OH)_2$-H_2O interfacial area diminishes, as well as the $Ca(OH)_2$ saturation index owing to calcite precipitation, $\eta(t)$ tends to decrease even before portlandite achieves undersaturation. Results show that at t = 0, $\eta(t)$ tends to be determined by $Ca(OH)_2$ solubility, which decreases with temperature (Figure 2C) and follows a bell shape with increasing salinity (Figure 2D). Figure 6 illustrates that the addition of NaCl does not significantly alter the pH during the step 1 process, maintaining a stable level of 13.2 in both the pure $Ca(OH)_2$ aqueous suspension and the NaCl-containing system.

The increase of $\eta(t)$ displayed by the sodium chloride- and sulfate-enhanced system during step 1 is promoted by enhancing the dissolution of CO_2 in aqueous solutions. Dennard[47] documented that the most effective catalysts for carbon dioxide hydration are oxyanions featuring lower oxidation states of nonmetals and possessing at least one lone pair of electrons, exemplified by ClO_4^- and SO_3^{2-}. These findings imply that the anions derived from common dissolved

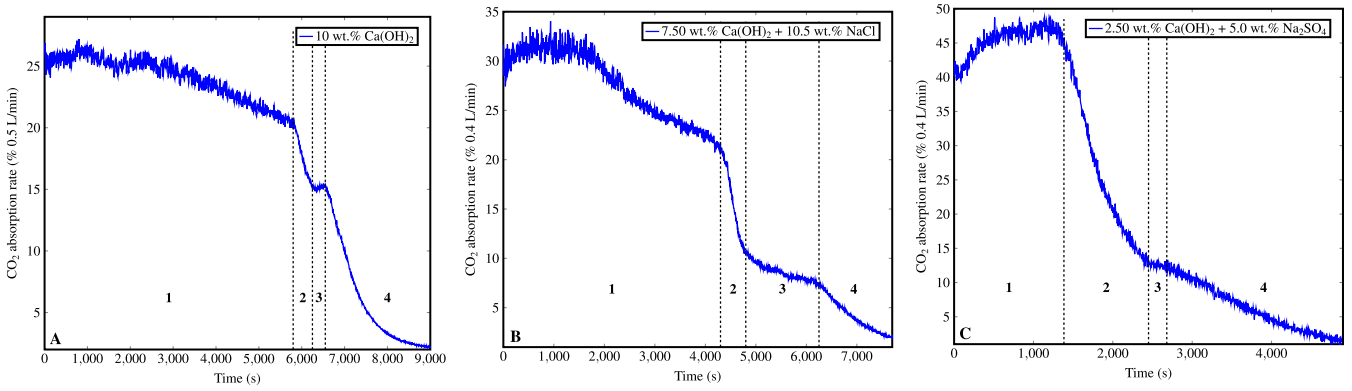

Figure 5. Typical CO_2 absorption rate (%) as a function of time curves for (A) pure $Ca(OH)_2$-H_2O−CO_2 system (exp. identifier: A5); (B) addition of NaCl impurities (exp. identifier: Na5); and (C) addition of Na_2SO_4 (exp. identifier: NaSO10).

https://doi.org/10.1021/acs.energyfuels.4c02455
Energy Fuels 2024, 38, 16678−16691

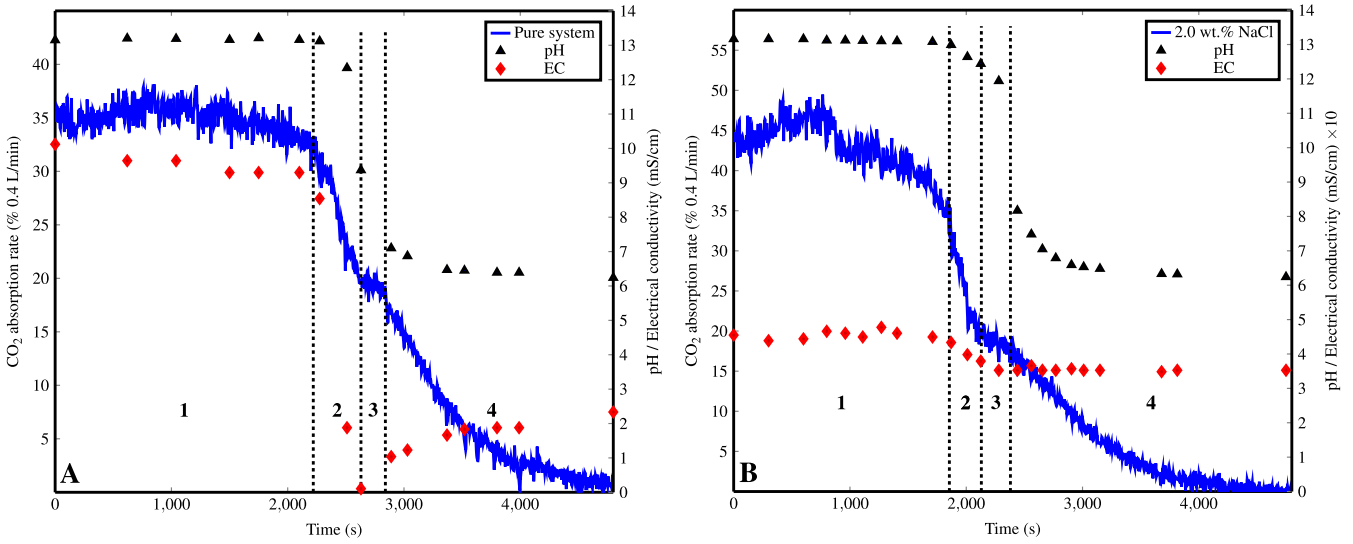

Figure 6. pH and EC measurements for (A) pure $Ca(OH)_2$-H_2O−CO_2 system (exp. identifier: Ca0) and (B) addition of NaCl (exp. identifier: NaCl9).

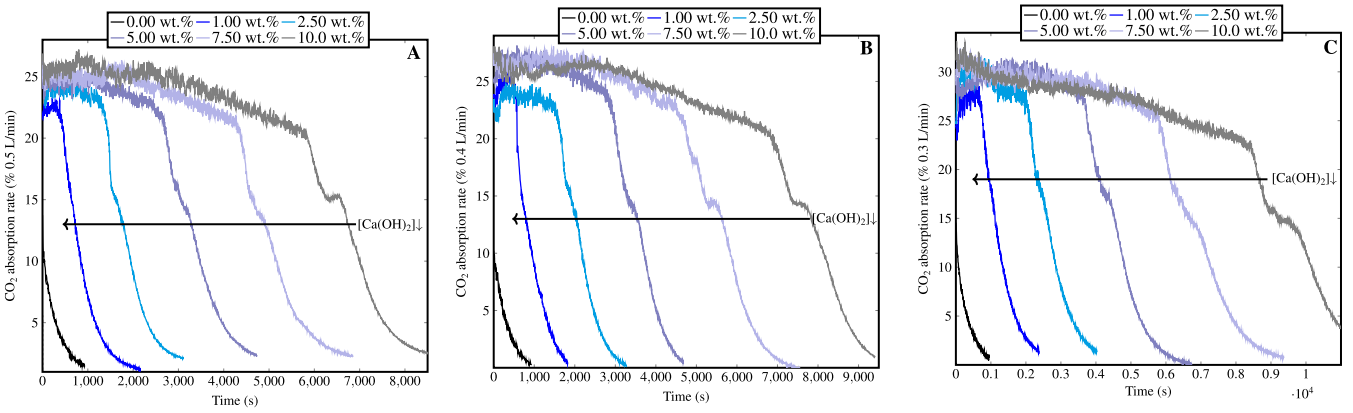

Figure 7. CO_2 absorption rate as a function of time for (A) experiments A0−5, (B) experiments B0−5, and (C) experiments C0−5.

salts investigated in this study may enhance the reaction between gaseous CO_2 and water, in keeping with one of the three proposed models by Dennard:[47] the direct interaction between CO_2 and the anion, interaction between water molecules neighboring CO_2 and the anion, or the anion acting as an electrophilic center. Discrepancies in the apparent rate control mechanisms during step 1 can be partly attributed to variations in gas−liquid interactions induced by the specific mode of action of each anion.

Step 2 is marked by a rapid decrease in $\eta(t)$, in combination with a gradual reduction of $Ca(OH)_2$ dissolution, leading to a diminution of Ca^{2+} supplied to the system. Step 3 is characterized by a secondary CO_2 absorption rate plateau, whose duration is linearly proportional to both the $Ca(OH)_2$ initial concentration and salinity, as detailed in Tables S3, 3, and S4. This plateau likely depends on the coarse $Ca(OH)_2$ particles, whose dissolution is slower than that of the finer ones. Therefore, the higher the NaCl initial concentration, the lower the CO_2 absorption rate of step 3 and the longer the plateau duration. At completion of steps 2 and 3, the measured pH and EC change from 13.2 to 7.1 and from 9299 to 105−1037 (red diamonds fall and rise), respectively, in the $Ca(OH)_2$-H_2O−CO_2 system. Overall, the observed pH and EC trends for the $Ca(OH)_2$-H_2O−CO_2 system were consistent with those from ref 48. A delay occurs between the decrease in $\eta(t)$ and the rapid decline in pH in the $Ca(OH)_2$-NaCl-H_2O−CO_2 system (Figure 6B) with its duration being proportional to that of step 3. Consequently, at the end of step 2, the pH is notably higher in the NaCl-containing system compared to that in the pure $Ca(OH)_2$ aqueous suspension. In this case, the measured pH and EC decrease from 13.1 to 7.05 and from 44.9 μS/cm to 35.3 mS/cm, respectively, with the higher EC value compared to the pure system attributed to the presence of dissolved NaCl. The EC decreases due to the reduction in the concentrations of OH^- and Ca^{2+} ions.

Finally, step 4 corresponds to the saturation of the solution with CO_2, as the blank experiments show when CO_2 is bubbled through ultrapure water (Figure 7). The CO_2 solubility and, consequently, the CO_2 uptake corresponding to this step increase with alkalinity. $\eta(t)$ gradually decreases to 0. The pH slowly declined to a minimum of 6.24 over the entire duration of these experiments. Overall, it was shown that the calibration between the measured CO_2 absorption rate $\eta(t)$ and pH enables continuous in situ pH monitoring directly via gas flow sensors.

3.4. Impact of Operational Parameters on CO_2 Absorption Rate during $Ca(OH)_2$ Aqueous Carbonation.

3.4.1. Impact of $Ca(OH)_2$ Concentration and CO_2 Flow Rate.

https://doi.org/10.1021/acs.energyfuels.4c02455
Energy Fuels 2024, 38, 16678−16691

Figure 7 illustrates $\eta(t)$ as a function of the $Ca(OH)_2$ concentration and the CO_2 flow rate. Table 2 details the

Table 2. Average CO_2 Absorption Rate, Standard Deviation, Duration, and Volume of Absorbed CO_2 for Step 1 of Experiments A1−5, B1−5, and C1−5

exp. identifier	$Ca(OH)_2$ wt %	$\overline{\eta_1}$ (%)	σ	t (s)	V_{CO_2} (L)
A1	1	21.3	0.44	420	0.74
A2	2.5	22.6	0.73	1410	2.65
A3	5	22.8	1.01	2730	5.19
A4	7.5	22.9	1.42	4400	8.40
A5	10	23.0	1.84	5930	11.35
B1	1	24.7	0.81	530	0.87
B2	2.5	23.4	0.71	1600	2.50
B3	5	25.9	1.13	2930	5.06
B4	7.5	25.5	1.61	4755	8.09
B5	10	24.4	2.05	7031	11.44
C1	1	27.0	1.27	723	0.98
C2	2.5	28.9	1.23	2025	2.93
C3	5	29.3	1.04	3725	5.46
C4	7.5	28.7	1.63	5931	8.50
C5	10	27.1	2.42	8531	11.57

average CO_2 absorption rate $\overline{\eta_1}$, step 1 durations, and volumetric CO_2 uptakes V_{CO_2} for the corresponding experiments. The initial CO_2 absorption rate, at low values of t, increases slightly with the increase of the $Ca(OH)_2$ concentration over the range of this study, in agreement with the literature.[49] Additionally, increasing the $Ca(OH)_2$ concentration linearly extends the durations of both step 1 and the secondary plateau (step 3), as detailed in Table S3 of the Supporting Information.

However, Table 2 shows that the $\overline{\eta_1}$ is not significantly affected by increasing the initial concentration of $Ca(OH)_2$, whereas the volume of CO_2 absorbed in step 1 increases slightly faster than the corresponding initial $Ca(OH)_2$ concentration. These results differ from those reported by Han[48] who observed that the excess of undissolved $Ca(OH)_2$ in the suspension significantly degraded the amount of absorbed CO_2 (g) and the CO_2 capture efficiency (%), suggesting that the simultaneous dissolution of $Ca(OH)_2$ and production of $CaCO_3$ hinder the association between Ca^{2+} and CO_3^{2-} in the suspension. These discrepancies are likely due to different data treatment methods, the higher L/S ratios (100−680) and lower $Ca(OH)_2$ loadings (0.73−5 g) in their study.

Furthermore, Figure 7 shows that excess calcite in the suspension slows the CO_2 absorption rate $\eta(t)$, as the $\eta(t)$ values at the end of step 1 decrease with increasing $Ca(OH)_2$ initial concentration. Several hypotheses may be formulated to explain this finding: (i) the excess calcite slows down the dissolution kinetics of CO_2 or $Ca(OH)_2$ and (ii) the excess calcite creates unreactive surfaces that hinder CO_3^{2-} or Ca^{2+} diffusion to the reactive sites.

The average CO_2 absorption rate $\overline{\eta_1}$ values increase with decreasing CO_2 flow rates, recording 21.3−23.0, 23.4−25.9, and 27.0−29.3% at CO_2 flow rates of 0.5, 0.4, and 0.3 L/min, respectively. However, the average carbonation durations simultaneously increase by 13.1 and 40.6%, resulting in equivalent CO_2 uptake for equivalent $Ca(OH)_2$ concentrations. In other words, increasing the gas flow rate reduces the carbonation time, as observed by several authors.[50]

3.4.2. Effects of the Temperature. The carbonation kinetics of portlandite are known to weakly depend on temperature, with reported apparent activation energies ranging approximately between 3 and 22 kJ/mol.[51] As shown earlier in Figure 3A, Phreeqc simulations point to a positive correlation between dissolution kinetics of $Ca(OH)_2$ and the temperature rise in the water column. This results in an increase of $\eta(t)$ up to 343 K, while the total uptake or the CO_2 volume absorbed during a whole experiment is slightly reduced due to the diminished CO_2 solubility. $\overline{\eta_1}$ exhibits a significant increase, from 19.5% at 283 K to 26.6% at 343 K, marking a 36.9% augmentation from the baseline. However, a further rise of temperature above 343 K does not result in a proportional increase in $\overline{\eta_1}$; instead, values lie in the range of 26.3−26.6%, at 343−363 K, as illustrated in Figure 8B. Notably, increasing the temperature beyond this point is expected to cause degassing

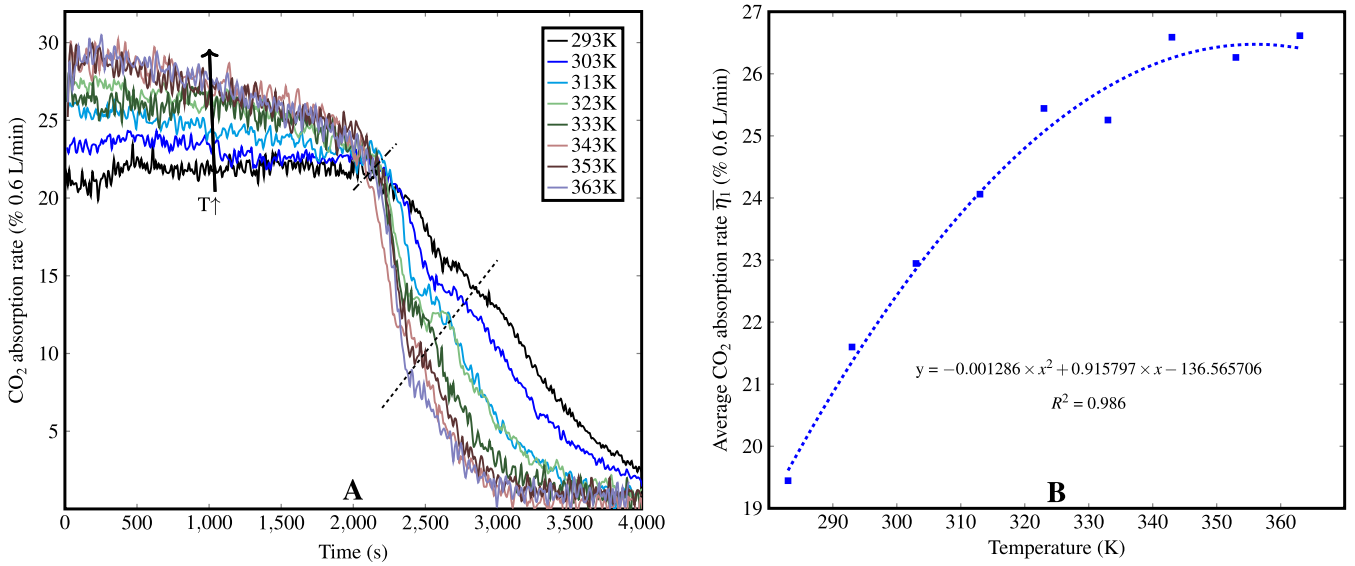

Figure 8. (A) CO_2 absorption rate as a function of time, for experiments T1−9. (B) Average CO_2 absorption rate calculated for step 1 as a function of the temperature.

https://doi.org/10.1021/acs.energyfuels.4c02455
Energy Fuels 2024, 38, 16678−16691

due to the solution exceeding its boiling point, which would consequently reduce the CO_2 absorption rate. Overall, the CO_2 absorption rate follows a polynomial trend with respect to temperature during $Ca(OH)_2$ aqueous carbonation, as displayed by Figure 8B. Additionally, the efficiency of $Ca(OH)_2$ conversion to $CaCO_3$ remains stable across temperature variations from 283 to 363 K, as observed by several authors.[52]

Typical temperatures inside field-scale carbonation reactors, ranging from 323 to 343 K, are a function of the temperature of the gas stream, the incoming solid and liquid reagent properties, and the effectiveness of insulation.[53] Our experiments reveal that relatively high flue gas temperatures at the reactor inlet are beneficial to enhancing reaction kinetics, although exceeding 343,000 K yields only marginal improvements.

3.4.3. Impact of NaCl Concentration. Table 3 presents the average CO_2 absorption rate, standard deviation, duration, and volume of absorbed CO_2 for each step in experiments NaCl1−6. Additionally, Table 4 provides detailed quantification of $\overline{\eta_1}$, $\overline{\eta_3}$, the duration, and the volume of absorbed CO_2 for step 3 in experiments NaCl7−20. As mentioned earlier, increasing NaCl concentration not only extends the secondary CO_2 absorption rate plateau of step 3 but also reduces the average CO_2 absorption rate $\overline{\eta_3}$, as demonstrated in Tables 3 and 4.

Table 3. Average CO_2 Absorption Rate, Standard Deviation, Duration, and Volume of Absorbed CO_2 for Each Step of Experiments NaCl1−6

exp. identifier		NaCl1	NaCl2	NaCl3	NaCl4	NaCl5	NaCl6
NaCl wt %		1	2	3.5	7	10.5	14
step 1.1	$\overline{\eta_{1,1}}$ (%)	31.4	34.3	35.74	34.6	31.0	23.7
	σ	0.98	0.91	1.37	1.03	0.95	2.62
	t (s)	2745	2125	2120	1830	1900	5275
	V_{CO_2} (L)	5.74	4.85	5.05	4.23	3.93	8.32
step 1.2	$\overline{\eta_{1,2}}$ (%)	26.8	29.7	31.7	27.7	24.7	
	σ	1.72	2.61	2.00	2.90	2.24	
	t (s)	1395	1725	1230	2060	2525	
	V_{CO_2} (L)	2.50	3.42	2.60	3.80	4.15	
step 2	$\overline{\eta_2}$(%)	17.5	17.5	21.0	16.2	13.9	12.3
	σ	2.31	3.36	5.04	3.74	2.78	2.54
	t (s)	345	435	705	470	410	425
	V_{CO_2} (L)	0.40	0.51	1.00	0.51	0.38	0.35
step 3	$\overline{\eta_3}$ (%)	12.9	11.8	11.2	9.1	8.5	6.9
	σ	1.43	0.93	0.77	0.98	0.85	0.82
	t (s)	860	840	780	1285	1535	1775
	V_{CO_2} (L)	0.74	0.67	0.58	0.78	0.87	0.81
step 4	$\overline{\eta_4}$(%)	4.5	4.7	4.7	4.4	4.6	3.5
	σ	2.44	2.71	2.75	1.48	1.14	0.91
	t (s)	1335	1440	1365	965	900	875
	V_{CO_2} (L)	0.40	0.45	0.42	0.29	0.27	0.20
total	V_{CO_2} (L)	9.78	9.88	9.64	9.60	9.60	9.68

Table 4. Average CO_2 Absorption Rate for Step 1 and Step 3, Duration, and Volume of Absorbed CO_2 for Step 3 of Experiments NaCl7−20

exp. identifier	[NaCl] (wt %)	average $\overline{\eta_1}$ (%)	average $\overline{\eta_3}$ (%)	t (s) step 3	V_{CO_2} (L) step 3
NaCl7	0.5	41.8	21.1	355	0.50
NaCl8	1	40.4	19.2	390	0.50
NaCl9	2	41.1	20.1	345	0.46
NaCl10	3	41.7	22.1	230	0.34
NaCl11	4	43.4	21.4	470	0.67
NaCl12	5	45.7	17.6	490	0.57
NaCl13	6	43.5	18.9	340	0.43
NaCl14	7	40.8	16.7	590	0.65
NaCl15	8	42.0	17.6	535	0.63
NaCl16	9	37.6	14.7	595	0.58
NaCl17	9.5	35.3	13.0	610	0.53
NaCl18	10	33.5	10.1	860	0.58
NaCl19	15	32.3	11.2	800	0.60
NaCl20	20	20.2	5.2	1180	0.41

Furthermore, the calculated average CO_2 absorption rate during step 1, $\overline{\eta_1}$, shows a significant increase, from 25.5% with pure $Ca(OH)_2$-H_2O solution to 35.74% with the addition of NaCl at 3.5 wt %, marking a 40% increment from the baseline. At higher NaCl concentrations, $\overline{\eta_1}$ starts to reduce, reaching the minimum of 23.6% at [NaCl] = 14 wt %. In general, $\overline{\eta_1}$ is positively affected by NaCl, but above some 4−5 wt %, a worsening begins. This behavior is likely ascribable to high NaCl concentration hindering the binding of Ca^{2+} to CO_3^{2-}, as suggested by Qian.[54] The authors found that the $CaCO_3$ crystallization rate constant decreased continuously when NaCl concentration increased from 3.5 to 14 wt %. Jo[55] also documented a progressive reduction in particle size at 1 M NaCl conditions and an increase at 2 M NaCl conditions for precipitated $CaCO_3$ in a cement aqueous carbonation system. Given the well-established inverse relationship between the $CaCO_3$ crystal size and nucleation frequency, the observed trend is in keeping with findings from the current study (Figure 9).

3.4.4. Impact of Common Salts: NaCl, KCl, Na_2SO_4, and K_2SO_4—A Comparison. Nicoleau[56] and Mesfin[57] explored recently the impacts of common cation chloride and sulfate concentrations on rate mechanisms in carbonation applications. Earlier, Xiang[28] studied the influence of chemical additives and static mixing on the formation of nanosized calcium carbonate.

As shown by Figure 10, the introduction of Na_2SO_4 at 55 g/kg of water (kgw) led to a notable enhancement of $\overline{\eta_1}$, reaching 51.2%, representing a substantial 75.7% increase from the baseline set at 29.2% for the pure $Ca(OH)_2$-H_2O−CO_2 system. Conversely, at 30 g/kgw NaCl, $\overline{\eta_1}$ values do not exceed 41.7%, yet corresponding to a substantial increase of 43.2% from the baseline. The highest enhancement of $\overline{\eta_1}$ at low concentration was observed with K_2SO_4, achieving a 49.1% increase at 30 g/kgw. This corresponds to an induced ionic strength of less than 0.65 mol/kgw. However, a sharp reduction emerged for an ionic strength of >0.65 mol/kgw; conversely, $\overline{\eta_1}$ keeps on increasing beyond this threshold using Na_2SO_4. This can be attributed to the lower solubility of potassium sulfate.

https://doi.org/10.1021/acs.energyfuels.4c02455
Energy Fuels 2024, 38, 16678−16691

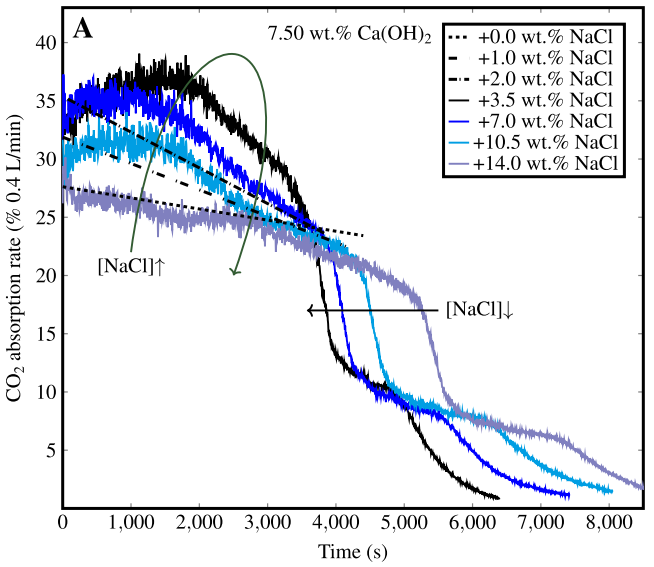

Figure 9. (A) CO_2 absorption rate as a function of time, experiments B4 and NaCl1−6. The 0.0, 1.0, and 2.0 wt % NaCl values represent the linear trendlines of step 1 in experiments B4 and NaCl1−2, shown only as dashed lines to limit the curve overlap.

The present results demonstrate that low to high concentrations of common Na/K-chlorides and sulfates have the potential to significantly enhance the mean CO_2 absorption rate $\overline{\eta_1}$ during $Ca(OH)_2$ carbonation. Maximum enhancement was observed between 3 and 6 wt % in the case of Na/K-chlorides. At lower and higher concentrations, the mean absorption rate $\overline{\eta_1}$ increased and then decreased, respectively, while the overall CO_2 uptake remains unaffected at reaction completion time. Additionally, higher $\overline{\eta_1}$ values were observed using NaCl in comparison with KCl.

With an optimal NaCl concentration of 3.5 wt %, seawater is therefore a relevant water source candidate to accelerate processes involving $Ca(OH)_2$ carbonation in coastal areas. However, the significant reductions in the CO_2 absorption rates observed at elevated concentrations of NaCl and KCl hold significant implications for IAW aqueous carbonation processes aiming at stabilizing potentially toxic heavy metals. Indeed, $Ca(OH)_2$ is the most reactive phase upon carbonation in many of these waste streams, along with other CCHO. The accumulation of leached Cl^- ions may diminish the efficiency of CO_2 removal from flue gas in the scenarios of wastewater reuse conditions and even impede the precipitation of carbonates due to the elevated solubility of calcium chloride phases.[57,58] The substantial leaching of Cl^- ions from IAW systems has been consistently observed across laboratory- and field-scale experiments, especially with waste incineration ashes.[59,60] Additionally, Miao[27] proposed the potential utilization of such wastewaters for the precipitation of chlorine salt products. To sustain a consistently high CO_2 absorption rate in regions facing water scarcity and requiring extensive water recycling to implement Ca-rich IAW carbonation cycles, a Cl^- extraction unit should be integrated.

The substantial enhancement of $\overline{\eta_1}$ observed at low ionic strength induced by K_2SO_4 holds significant implications for process efficiency. This is particularly relevant in the context of utilizing phosphogypsum waste for the CO_2 mineral sequestration. By reacting KOH with $CaSO_4{\cdot}2H_2O$ (gypsum), it is possible to obtain K_2SO_4 and $CaCO_3$ via the formation of $Ca(OH)_2$.[61,62]

Finally, the highest $\overline{\eta_1}$ enhancement was observed using Na_2SO_4 with a substantial 90.8% increase from the baseline at 75 g/kgw [Na_2SO_4]. This finding underscores the potential of using sodium sulfate to improve calcium hydroxide carbonation processes. The superiority of Na_2SO_4 over NaCl suggests a specific interaction mode of sulfate ions with the $H_2O-CO_2-Ca(OH)_2$-CO_2 system compared to chloride ions, particularly at higher salt concentrations, as evidenced by the clear differentiation of Na_2SO_4 and NaCl cloud points when the ionic strength exceeded 0.8 mol/kgw. Few studies in the literature have explored the interaction between Na_2SO_4 and aqueous carbonation systems. Liu[63] observed significant carbonation depth in FA and Portland cement concretes

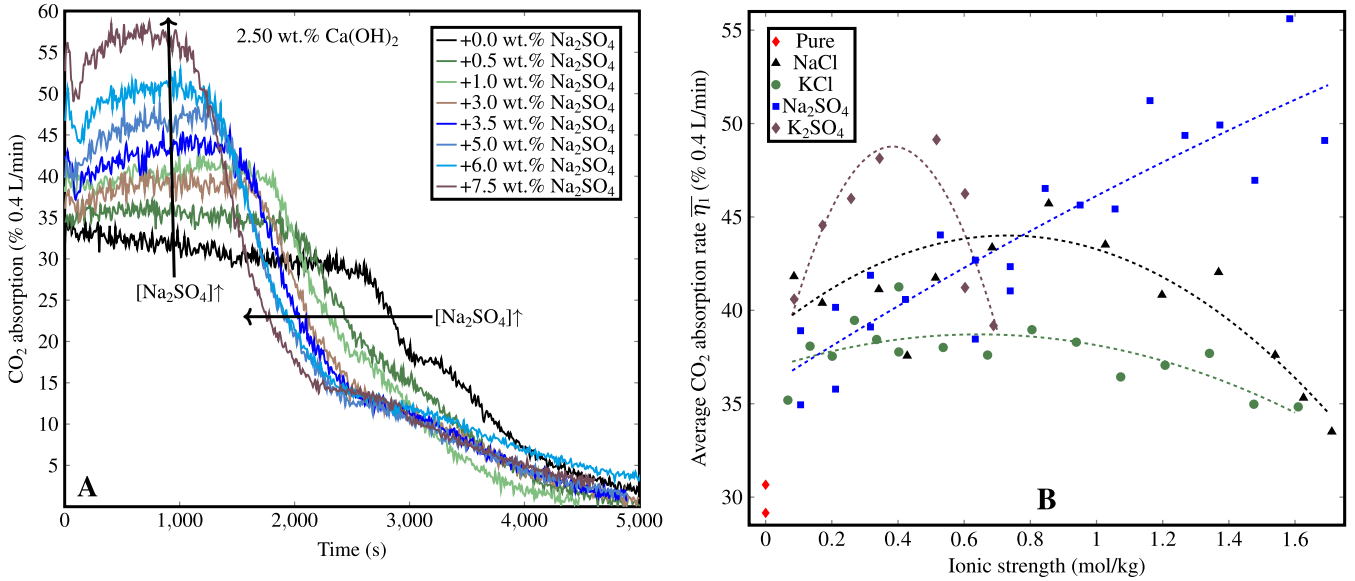

Figure 10. (A) CO_2 absorption rate as a function of time, for experiments NaSO1−14, and (B) average CO_2 absorption rate as a function of ionic strength for the pure $Ca(OH)_2$-H_2O-CO_2 system compared to NaCl, KCl, Na_2SO_4, and K_2SO_4 enhanced systems.

https://doi.org/10.1021/acs.energyfuels.4c02455
Energy Fuels 2024, 38, 16678−16691

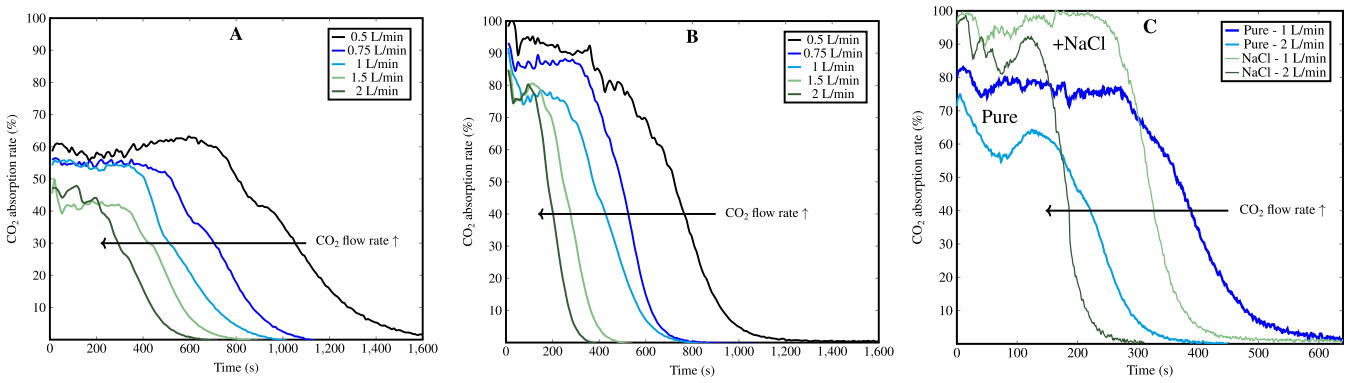

Figure 11. CO_2 absorption rate as a function of time (s) for CO_2 flow rates ranging between 0.5 and 2 L/min using a sparger, without (A, experiments SPR1 and SPR5) and with (B, experiments SPR_Na1 and SPR5) NaCl at 3.5 wt %. Graph (C) is equivalent for CO_2 flow rates equal to 1 and 2 L/min using a porous stone diffusor, experiments Diff1−4.

exposed to a 10% Na_2SO_4 solution, highlighting the rapid carbonation of $Ca(OH)_2$ in the presence of Na_2SO_4. In line with our findings, recent research by Zajac[64] demonstrates that Na_2SO_4 significantly accelerates calcium carbonate precipitation during cement paste aqueous carbonation, although the precise mechanism is yet to be elucidated.

3.4.5. Impact of the Static Gas−Liquid Mixing System: Pipe, Sparger, and Diffusor. Figure 11 and Table 5 illustrate

Table 5. Average CO_2 Absorption Rate, Standard Deviation, Duration, and Volume of Absorbed CO_2 for Step 1 of Experiments SPR1−5, SPR_Na1−5, and Diff1−4

exp. identifier	CO_2 flow (L/min)	$\overline{\eta_1}$ (%)	σ	t (s)	V_{CO_2} (L)
SPR1	0.5	59.8	2.13	749	3.73
SPR2	0.75	54.3	1.53	521	3.54
SPR3	1	53.7	1.76	420	3.76
SPR4	1.5	41.7	2.21	368	3.84
SPR5	2	44.1	2.99	252	3.71
SPR_Na1	0.5	89.7	5.88	502	3.75
SPR_Na2	0.75	86.9	2.23	353	3.83
SPR_Na3	1	77.0	4.73	298	3.83
SPR_Na4	1.5	78.2	4.00	181	3.54
SPR_Na5	2	77.4	3.45	140	3.61
Diff1	1	77.0	2.29	288	3.70
Diff2	2	61.8	4.84	178	3.67
Diff3	1	96.5	2.67	257	4.13
Diff4	2	89.0	4.51	131	3.89

the impact of enhancing the system with a sparger and diffusor. Using the sparger configuration, the average CO_2 absorption rate, $\overline{\eta_1}$, ranges between 44.1 and 59.8% without NaCl and 77 and 89.7%, with NaCl at 3.5 wt %. Increasing the CO_2 flow from 0.5 to 2 L/min results in a modest reduction of $\overline{\eta_1}$ from the baseline of 26.2 and 13.7% without and with NaCl, respectively. Notably, adding NaCl proves to be more effective at higher CO_2 flow rates: enhancing $\overline{\eta_1}$ by 50% from SPR1 to SPR_Na1 and by 75.5% from SPR5 to SPR_Na5. In the diffusor configuration, the average CO_2 absorption rate $\overline{\eta_1}$ ranges from 61.8 to 77% without NaCl and increases to 89−96.5% with NaCl at 3.5 wt %. Similar to the sparger configuration (Figure 1, configuration 3), $\overline{\eta_1}$ decreased with rising CO_2 flow rates. Remarkably, experiment Diff3 recorded the highest value across the study with an average CO_2 absorption rate reaching nearly 96.5%.

The $Ca(OH)_2$ dissolution, the CO_2 dissolution kinetics, and diffusion are widely considered primary rate-controlling steps for portlandite carbonation. Using static mixers, a porous stone diffusor, and a sparger rather than a simple pipe leads to an increase of the CO_2−water interfacial surface area by reducing the size of the bubbles, in addition to an increase of the gas residence time, thus triggering a cascade of kinetic acceleration of dissolution. The homogeneous dissolution of CO_2, which locally reduces pH and therefore promotes the dissolution of $Ca(OH)_2$, can therefore be considered a primary rate-controlling process.

Furthermore, among the tested static gas−liquid mixer, the porous stone diffusor can eliminate energy consumption attributed to mixing tools such as a stirrer or an impeller by effectively harnessing the turbulence induced by the bubbles from the bottom of the reactor. Still, care should be paid to prevent the blocking of the sparger holes when using such mixing tools in a gas−solid−liquid system. Said[65] proposed a potential solution by a sparger pointing downward, positioned 5 cm above the bottom of the reactor, in the case of a pilot-scale steelmaking slag carbonation system. Besides, it is crucial to consider the pressure loss associated with the gas flow through a porous material. This pressure drop can significantly impact the overall efficiency and effectiveness of the mixing process. Proper evaluation and compensation for this pressure loss are essential to maintain optimal operational conditions and achieve the desired reaction outcomes in the reactor on a field scale.

Additionally, the liquid-to-solid ratios between portlandite and water investigated in this study range between 10 and 66.7, which are considered from high to very high values for ex situ carbonation systems. However, it is a shared opinion that the optimum carbonation L/S ratio lies between 0.2 and 0.3, especially for IAW case studies.[66] In closed systems where CO_2 (gas phase) does not exhibit convection between the reactor inlet and outlet, these considerations may be true. However, they neglect the complex thermo-hydro-mechanical-chemical (THMC) interplays in open systems where CO_2 flows continuously. The reduction in internal CO_2 mobility within the reactor, caused by water viscosity slowing the CO_2 diffusion, can be easily countered by employing a combination of static and dynamic mixers, as demonstrated in this study. Consequently, classical models like the shrinking core model are incomplete at high L/S ratios with well-diffused CO_2, turbulent conditions, and small particles. Instead, advanced

https://doi.org/10.1021/acs.energyfuels.4c02455
Energy Fuels 2024, 38, 16678−16691

models incorporating multiple mechanisms, including mass transfer with reaction kinetics, yield more accurate predictions.[5]

4. CONCLUSIONS

Our investigation provides insights into the influence of the operational parameters on the CO_2 absorption rate $\eta(t)$ in the $Ca(OH)_2$ aqueous carbonation process. Temperature is a key parameter, leading to a slight increase in $\overline{\eta_1}$ from 19.5% at 283 K to 26.6% at 343 K, marking a 36.9% improvement from the baseline. Exceeding 343 K yields marginal improvements to $\eta(t)$.

The introduction of NaCl at 3.5 wt % provides a notable 34.2% increase in $\overline{\eta_1}$. In particular, adding 3.5 wt % [NaCl] proves more effective at higher CO_2 flow rates and enhances CO_2 diffusion, increasing $\overline{\eta_1}$ by 50 and 75.5% in the sparger configuration at 0.5 and 2 L/min, respectively. With an optimal NaCl concentration of 3.5 wt %, seawater is therefore a candidate to improve the CO_2 capture process involving calcium hydroxide carbonation in coastal areas.

Additionally, the study describes how the reduction in internal CO_2 mobility within a high liquid-to-solid ratio, caused by water viscosity slowing CO_2 diffusion, can be easily countered by employing a combination of static and dynamic mixers. Remarkably, porous stone diffusers prove to be highly effective, accelerating dissolution kinetics and achieving absorption rates exceeding 96% and nearing 90%, respectively, at 1 and 2 L/min CO_2 flow, while also canceling energy consumption due to mixing.

Furthermore, Na_2SO_4 is the most efficient among tested salts (NaCl, KCl, K_2SO_4, Na_2SO_4) in enhancing $\eta(t)$, with a substantial 75% increase at 55 g/kgw [Na_2SO_4]. The superiority of Na_2SO_4 over NaCl indicates that sulfate ions promote the dissolution of CO_2 in aqueous solutions more efficiently than chloride ions do.

This research holds potential for the design of more efficient reactors tailored for ex situ carbon capture, both "at the smokestack" and in the domain of direct air capture. Notably, quantifying the impact of salts such as NaCl or Na_2SO_4 on CO_2 absorption rates through enhanced CO_2 dissolution kinetics entails massive implications, particularly for alternative water sources such as wastewaters and seawater. Research is ongoing to gain further insights into these mechanisms.

■ ASSOCIATED CONTENT

Supporting Information

The Supporting Information is available free of charge at https://pubs.acs.org/doi/10.1021/acs.energyfuels.4c02455.

Detailed experimental parameters for the studies with their corresponding experiment identifiers, methodology to structure numerically the CO_2 absorption vs time patterns into distinct steps, review of the experimental conditions, investigated parameters, and most relevant conclusions for the $Ca(OH)_2$ carbonation at the lab scale, Phreeqc scripts to reproduce the models, SEM images of the portlandite particles, the diffusor, and the sparger surface/matrix, schematic representation of the suggested reaction mechanisms for $Ca(OH)_2$ aqueous carbonation in a pure solution and in the presence of NaCl, and $Ca(OH)_2$ solubility and dissolution kinetic results from Phreeqc simulations (PDF)

■ AUTHOR INFORMATION

Corresponding Author

Quentin Wehrung − *Earth Science Department, University of Turin, 10125 Torino, Italy;* orcid.org/0000-0002-5332-5154; Phone: +33 663281762; Email: quentin.wehrung@unito.it

Authors

Linda Pastero − *Earth Science Department, University of Turin, 10125 Torino, Italy;* orcid.org/0000-0002-9453-9503

Davide Bernasconi − *Earth Science Department, University of Turin, 10125 Torino, Italy*

Andrea Cotellucci − *Earth Science Department, University of Turin, 10125 Torino, Italy;* orcid.org/0000-0003-2027-3260

Marco Bruno − *Earth Science Department, University of Turin, 10125 Torino, Italy;* orcid.org/0000-0002-0161-574X

Simona Cavagna − *Earth Science Department, University of Turin, 10125 Torino, Italy*

Enrico Destefanis − *Earth Science Department, University of Turin, 10125 Torino, Italy*

Caterina Caviglia − *Earth Science Department, University of Turin, 10125 Torino, Italy*

Alessandro Pavese − *Earth Science Department, University of Turin, 10125 Torino, Italy*

Complete contact information is available at: https://pubs.acs.org/10.1021/acs.energyfuels.4c02455

Notes

The authors declare no competing financial interest.

■ ACKNOWLEDGMENTS

This research was funded by ECOSPRAY TECHNOLOGIES S.r.l., Italian Ministry for Education, University and Research (MIUR; project PRIN2017-2017L83S77), and Ministry for Ecological Transition (MiTE; project CLEAN) for possible applications to fly ash treatment.

■ ABBREVIATIONS

AWL	accelerated weathering of limestone
APCr	air pollution control residues
BET	Brunauer−Emmett−Teller
CaL	calcium looping
CCHO	calcium (chloro)(hydr-)oxides
CCS	carbon capture and storage
CCR	calcium carbide residues
CKD	cement kiln dusts
DAC	direct air capture
EC	electrolytical conductivity
EDS	energy dispersive X-ray spectroscopy
FA	fly ash
HCFA	high-calcium coal fly ashes
IAW	industrial alkaline wastes
kgw	kilogram of water
m	molality (mol/kg)
SEM	scanning electron microscopy
SI	saturation index
SSA	specific surface area
THMC	thermo-hydro-mechanical-chemical
WPFA	waste paper fly ashes

XRPD X-ray powder diffraction

REFERENCES

(1) Gerdemann, S. J.; O'Connor, W. K.; Dahlin, D. C.; Penner, L. R.; Rush, H. Ex situ aqueous mineral carbonation. *Environ. Sci. Technol.* **2007**, *41* (7), 2587−2593.

(2) Kalinkin, A. M.; Kalinkina, E. V.; Zalkind, O. A.; Makarova, T. I. Chemical interaction of calcium oxide and calcium hydroxide with CO_2 during mechanical activation. *Inorg. Mater.* **2005**, *41*, 1073−1079.

(3) Gupta, H.; Fan, L. S. Carbonation−calcination cycle using high reactivity calcium oxide for carbon dioxide separation from flue gas. *Ind. Eng. Chem. Res.* **2002**, *41* (16), 4035−4042.

(4) Pan, S. Y.; Chang, E. E.; Chiang, P. C. CO_2 capture by accelerated carbonation of alkaline wastes: a review on its principles and applications. *Aerosol Air Qual. Res.* **2012**, *12* (5), 770−791.

(5) Bobicki, E. R.; Liu, Q.; Xu, Z.; Zeng, H. Carbon capture and storage using alkaline industrial wastes. *Prog. Energy Combust. Sci.* **2012**, *38* (2), 302−320.

(6) Bodor, M.; Santos, R. M.; Van Gerven, T.; Vlad, M. Recent developments and perspectives on the treatment of industrial wastes by mineral carbonation—a review. *Cent. Eur. J. Eng.* **2013**, *3*, 566−584.

(7) Ho, H. J.; Iizuka, A.; Lee, C. H.; Chen, W. S. Mineral carbonation using alkaline waste and byproducts to reduce CO_2 emissions in Taiwan. *Environ. Chem. Lett.* **2023**, *21* (2), 865−884.

(8) Renforth, P. The negative emission potential of alkaline materials *Nat. Commun. 10* 11401 .

(9) Sorrentino, G. P.; Zanoletti, A.; Ducoli, S.; Zacco, A.; Iora, P.; Invernizzi, C. M.; Bontempi, E. Accelerated and natural carbonation of a municipal solid waste incineration (MSWI) fly ash mixture: Basic strategies for higher carbon dioxide sequestration and reliable mass quantification. *Environ. Res.* **2023**, *217*, No. 114805.

(10) Huntzinger, D. N.; Gierke, J. S. Mineral carbonation for carbon sequestration in cement kiln dust from waste piles. *J. Hazard. Mater.* **2009**, *168* (1), 31−37.

(11) Bodor, M.; Santos, R. M.; Kriskova, L.; Elsen, J.; Vlad, M.; Van Gerven, T. Susceptibility of mineral phases of steel slags towards carbonation: mineralogical, morphological and chemical assessment. *Eur. J. Mineral.* **2013**, *25* (4), 533−549.

(12) Biava, G.; Zacco, A.; Zanoletti, A.; Sorrentino, G. P.; Capone, C.; Principallo, A.; Bontempi, E. Accelerated Direct Carbonation of Steel Slag and Cement Kiln Dust: An Industrial Symbiosis Strategy Applied in the Bergamo−Brescia Area. *Materials* **2023**, *16* (11), 4055.

(13) Zhang, N.; Huang, H. D.; Yang, R.; Zheng, A.; Moment, A. Aqueous metal ion leaching processes from high sulfur coal fly ash for carbon mineralization: The importance of pH control on cation extraction, carbonate purity, and silicon Q structure. *Chem. Eng. J.* **2023**, *474*, No. 145968.

(14) Bouzar, B.; Mamindy-Pajany, Y.; Mkahal, Z.; Benzerzour, M.; Abriak, N. E. Pilot-scale natural carbonation of waste paper fly ash for stabilization of Ba and Pb. *Green Technol. Sustain.* **2024**, *2* (2), No. 100075.

(15) Chindaprasirt, P.; Jaturapitakkul, C.; Tangchirapat, W.; Jitsangiam, P.; Nuithitikul, K.; Rattanasak, U. Carbon dioxide capture with aqueous calcium carbide residual solution for calcium carbonate synthesis and its use as an epoxy resin filler. *Eur. J. Mineral.* **2023**, *345*, No. 118783.

(16) Gunning, P. J.; Hills, C. D.; Carey, P. J. Production of lightweight aggregate from industrial waste and carbon dioxide. *Waste Manage.* **2009**, *29* (10), 2722−2728.

(17) Montes-Hernandez, G.; Concha-Lozano, N.; Renard, F.; Quirico, E. Removal of oxyanions from synthetic wastewater via carbonation process of calcium hydroxide: Applied and fundamental aspects. *J. Hazard. Mater.* **2009**, *166* (2−3), 788−795.

(18) Hamdouni, A.; Montes-Hernandez, G.; Tlili, M.; Findling, N.; Renard, F.; Putnis, C. V. Removal of Fe (II) from groundwater via aqueous portlandite carbonation and calcite-solution interactions. *Chem. Eng. J.* **2016**, *283*, 404−411.

(19) Ni, P.; Xiong, Z.; Tian, C.; Li, H.; Zhao, Y.; Zhang, J.; Zheng, C. Influence of carbonation under oxy-fuel combustion flue gas on the leachability of heavy metals in MSWI fly ash. *Waste Manage.* **2017**, *67*, 171−180.

(20) Habte, L.; Shiferaw, N.; Thriveni, T.; Mulatu, D.; Lee, M. H.; Jung, S. H.; Ahn, J. W. Removal of Cd(II) and Pb (II) from wastewater via carbonation of aqueous Ca $(OH)_2$ derived from eggshell. *Process Saf. Environ. Prot.* **2020**, *141*, 278−287.

(21) Yuan, B.; Hu, H.; Huang, Y.; Guo, G.; Gong, L.; Zou, C.; Yao, H. Effect of hydrated lime on the migration behavior of selenium in the MSWI plants: Experimental and theoretical study. *Chem. Eng. J.* **2022**, *433*, No. 134603.

(22) Qin, J.; Zhang, Y.; Yi, Y.; Fang, M. Carbonation of municipal solid waste gasification fly ash: effects of pre-washing and treatment period on carbon capture and heavy metal immobilization. *Environ. Pollut.* **2022**, *308*, No. 119662.

(23) Rau, G. H. CO_2 mitigation via capture and chemical conversion in seawater. *Environ. Sci. Technol.* **2011**, *45* (3), 1088−1092.

(24) Caserini, S.; Cappello, G.; Righi, D.; Raos, G.; Campo, F.; De Marco, S.; Grosso, M. Buffered accelerated weathering of limestone for storing CO_2: Chemical background. *Int. J. Greenhouse Gas Control* **2021**, *112*, No. 103517.

(25) Gislason, S. R.; Wolff-Boenisch, D.; Stefansson, A.; Oelkers, E. H.; Gunnlaugsson, E.; Sigurdardottir, H.; Fridriksson, T. Mineral sequestration of carbon dioxide in basalt: A pre-injection overview of the CarbFix project. *Int. J. Greenhouse Gas Control* **2010**, *4* (3), 537−545.

(26) Richardson, K.; Steffen, W.; Lucht, W.; Bendtsen, J.; Cornell, S. E.; Donges, J. F.; Rockström, J. Earth beyond six of nine planetary boundaries. *Sci. Adv.* **2023**, *9* (37), No. eadh2458.

(27) Miao, E.; Du, Y.; Zheng, X.; Zhang, X.; Xiong, Z.; Zhao, Y.; Zhang, J. CO_2 sequestration by direct mineral carbonation of municipal solid waste incinerator fly ash in ammonium salt solution: Performance evaluation and reaction kinetics. *Sep. Purif. Technol.* **2023**, *309*, No. 123103.

(28) Xiang, L.; Xiang, Y.; Wang, Z. G.; Jin, Y. Influence of chemical additives on the formation of super-fine calcium carbonate. *Powder Technol.* **2002**, *126* (2), 129−133.

(29) Chakraborty, D.; Bhatia, S. K. Formation and aggregation of polymorphs in continuous precipitation. 2. Kinetics of $CaCO_3$ precipitation. *Ind. Eng. Chem. Res.* **1996**, *35* (6), 1995−2006.

(30) Lee, D. K. An apparent kinetic model for the carbonation of calcium oxide by carbon dioxide. *Chem. Eng. J.* **2004**, *100* (1−3), 71−77.

(31) Mitchell, M. J.; Jensen, O. E.; Cliffe, K. A.; Maroto-Valer, M. M. A model of carbon dioxide dissolution and mineral carbonation kinetics. *Proc. R. Soc. A* **2010**, *466* (2117), 1265−1290.

(32) Izadifar, M.; Ukrainczyk, N.; Salah Uddin, K. M.; Middendorf, B.; Koenders, E. Dissolution of Portlandite in pure water: part 2 atomistic kinetic Monte Carlo (KMC) approach. *Materials* **2022**, *15* (4), 1442.

(33) Parkhurst, D. L.; Appelo, C. A. Description of input and examples for PHREEQC version 3—a computer program for speciation, batch-reaction, one-dimensional transport, and inverse geochemical calculations. *US Geol. Surv. Technol. Methods* **2013**, *6* (A43), 497.

(34) Lu, P.; Zhang, G.; Apps, J.; Zhu, C. Comparison of thermodynamic data files for PHREEQC. *Earth-Sci. Rev.* **2022**, *225*, No. 103888.

(35) Rahmani, O.; Kadkhodaie, A.; Highfield, J. Kinetics analysis of CO_2 mineral carbonation using byproduct red gypsum. *Energy Fuels* **2016**, *30* (9), 7460−7464.

(36) Zhang, Y.; Hu, B.; Teng, Y.; Tu, K.; Zhu, C. A library of BASIC scripts of reaction rates for geochemical modeling using phreeqc. *Comput. Geosci.* **2019**, *133*, No. 104316.

(37) Wang, J. U.; Keener, T. C.; Li, G.; Khang, S. J. The dissolution rate of Ca $(OH)_2$ in aqueous solutions. *Chem. Eng. Commun.* **1998**, *169* (1), 167−184.

https://doi.org/10.1021/acs.energyfuels.4c02455
Energy Fuels 2024, 38, 16678−16691

(38) Kutus, B.; Gácsi, A.; Pallagi, A.; Pálinkó, I.; Peintler, G.; Sipos, P. A comprehensive study on the dominant formation of the dissolved Ca $(OH)_2$(aq) in strongly alkaline solutions saturated by Ca(II). *RSC Adv.* **2016**, *6* (51), 45231−45240.
(39) Johnston, J.; Grove, C. The solubility of calcium hydroxide in aqueous salt solutions. *J. Am. Chem. Soc.* **1931**, *53* (11), 3976−3991.
(40) Li, Y. H.; Tsui, T. F. The solubility of CO_2 in water and sea water. *J. Geophys. Res.* **1971**, *76* (18), 4203−4207.
(41) De Visscher, A.; Vanderdeelen, J.; Königsberger, E.; Churagulov, B. R.; Ichikuni, M.; Tsurumi, M. IUPAC-NIST solubility data series. 95. Alkaline earth carbonates in aqueous systems. Part 1. Introduction, Be and Mg. *J. Phys. Chem. Ref. Data* **2012**, *41* (1), No. 013105.
(42) Ruiz-Agudo, E.; Kudłacz, K.; Putnis, C. V.; Putnis, A.; Rodriguez-Navarro, C. Dissolution and carbonation of portlandite [$Ca(OH)_2$] single crystals. *Environ. Sci. Technol.* **2013**, *47* (19), 11342−11349.
(43) Regnault, O.; Lagneau, V.; Schneider, H. Experimental measurement of portlandite carbonation kinetics with supercritical CO_2. *Chem. Geol.* **2009**, *265* (1−2), 113−121.
(44) Tiefenthaler, J.; Mazzotti, M. Experimental Investigation of a Continuous Reactor for CO_2 Capture and $CaCO_3$ Precipitation. *Front. Chem. Eng.* **2022**, *4*, No. 830284.
(45) Johannsen, K.; Rademacher, S. Modelling the kinetics of calcium hydroxide dissolution in water. *Acta Hydrochim. Hydrobiol.* **1999**, *27* (2), 72−78.
(46) Van Balen, K. Carbonation reaction of lime, kinetics at ambient temperature. *Cem. Concr. Res.* **2005**, *35* (4), 647−657.
(47) Dennard, A. E.; Williams, R. J. The catalysis of the reaction between carbon dioxide and water. *J. Chem. Soc. A* **1966**, 812−816.
(48) Han, S. J.; Yoo, M.; Kim, D. W.; Wee, J. H. Carbon dioxide capture using calcium hydroxide aqueous solution as the absorbent. *Energy Fuels* **2011**, *25* (8), 3825−3834.
(49) Kojima, H.; Hakuta, M.; Kudoh, K.; Ichinoseki, T.; Midorikawa, H. Chemical absorption into slurry in gas-sparged stirred vessel under continuous operation. *J. Chem. Eng. Jpn.* **1989**, *22* (6), 621−627.
(50) Harja, M.; Cretescu, I.; Rusu, L.; Ciocinta, R. C. The influence of experimental factors on calcium carbonate morphology prepared by carbonation. *Rev. Chim.* **2009**, *60*, 1258−1263.
(51) Falzone, G.; Mehdipour, I.; Neithalath, N.; Bauchy, M.; Simonetti, D.; Sant, G. New insights into the mechanisms of carbon dioxide mineralization by portlandite. *AIChE J.* **2021**, *67* (5), No. e17160.
(52) Montes-Hernández, G.; Renard, F.; Geoffroy, N.; Charlet, L.; Pironon, J. Calcite precipitation from CO_2−H_2O−Ca $(OH)_2$ slurry under high pressure of CO_2. *J. Cryst. Growth* **2007**, *308* (1), 228−236.
(53) Reynolds, B.; Reddy, K. J.; Argyle, M. D. Field application of accelerated mineral carbonation. *Minerals* **2014**, *4* (2), 191−207.
(54) Qian, M.; Zuo, Y.; Chen, Z.; Yin, X.; Liu, Y.; Yang, W.; Chen, Y. Crystallization of $CaCO_3$ in aqueous solutions with extremely high concentrations of NaCl. *Crystals* **2019**, *9* (12), 647.
(55) Jo, H.; Jang, Y. N.; Jo, H. Y. Influence of NaCl on mineral carbonation of CO_2 using cement material in aqueous solutions. *Chem. Eng. Sci.* **2021**, *80*, 232−241.
(56) Nicoleau, L.; Schreiner, E.; Nonat, A. Ion-specific effects influencing the dissolution of tricalcium silicate. *Cem. Concr. Res.* **2014**, *59*, 118−138.
(57) Mesfin, K. G.; Wolff-Boenisch, D.; Gislason, S. R.; Oelkers, E. H. Effect of Cation Chloride Concentration on the Dissolution Rates of Basaltic Glass and Labradorite: Application to Subsurface Carbon Storage. *Minerals* **2023**, *13* (5), 682.
(58) Liu, Z.; Yang, Y.; Zhang, Y.; Yue, Y.; Zhang, J.; Qian, G. Controlling role of CaClOH in the process of dechlorination for municipal solid incineration fly ash utilization. *ACS ES&T Eng.* **2022**, *2* (11), 2150−2158.
(59) Benassi, L.; Pasquali, M.; Zanoletti, A.; Dalipi, R.; Borgese, L.; Depero, L. E.; Bontempi, E. Chemical stabilization of municipal solid waste incineration fly ash without any commercial chemicals: first pilot-plant scaling up. *ACS Sustainable Chem. Eng.* **2016**, *4* (10), 5561−5569.
(60) Alam, Q.; Lazaro, A.; Schollbach, K.; Brouwers, H. J. Chemical speciation, distribution and leaching behavior of chlorides from municipal solid waste incineration bottom ash. *Chemosphere* **2020**, *241*, No. 124985.
(61) Lachehab, A.; Mertah, O.; Kherbeche, A.; Hassoune, H. Utilization of phosphogypsum in CO_2 mineral sequestration by producing potassium sulphate and calcium carbonate. *Mater. Sci. Energy Technol.* **2020**, *3*, 611−625.
(62) Bouargane, B.; Biyoune, M. G.; Mabrouk, A.; Bachar, A.; Bakiz, B.; Ait Ahsaine, H.; Atbir, A. Experimental investigation of the effects of synthesis parameters on the precipitation of calcium carbonate and portlandite from Moroccan phosphogypsum and pure gypsum using carbonation route. *Waste Biomass Valorization* **2020**, *11*, 6953−6965.
(63) Liu, Z.; Hu, W.; Hou, L.; Deng, D. Effect of carbonation on physical sulfate attack on concrete by Na_2SO_4. *Constr. Build. Mater.* **2018**, *193*, 211−220.
(64) Zajac, M.; Skibsted, J.; Lothenbach, B.; Bullerjahn, F.; Skocek, J.; Haha, M. B. Effect of sulfate on CO_2 binding efficiency of recycled alkaline materials. *Cem. Concr. Res.* **2022**, *157*, No. 106804.
(65) Said, A.; Laukkanen, T.; Järvinen, M. Pilot-scale experimental work on carbon dioxide sequestration using steelmaking slag. *Appl. Energy* **2016**, *177*, 602−611.
(66) Wang, L.; Jin, Y.; Nie, Y. Investigation of accelerated and natural carbonation of MSWI fly ash with a high content of Ca. *J. Hazard. Mater.* **2010**, *174* (1−3), 334−343.

https://doi.org/10.1021/acs.energyfuels.4c02455
Energy Fuels 2024, 38, 16678−16691